Painting and Direct Writing of Silver Nanostructures on Phosphate Glass with Electron Beam Irradiation

*Kyle E. Jacobs and Placid M. Ferreira**

Surfaces with silver nanostructures are useful, due to their potential to resonate strongly with visible light. This report demonstrates a process for the directed extraction of silver at the surface of a transparent superionic conductor. A focused electron beam incident on superionic $AgIAgPO_3$ glass results in localized negative charge deposition, which is neutralized by the electrochemical reduction of free silver ions. This process was characterized for beam energies ranging from 1 to 12 kV and primary beam fluence ranging from 50 pC μm^{-2} to 35 nC μm^{-2}. For electron fluence less than 2.5 nC μm^{-2} the process produces vibrant coloration of the glass which can be tuned throughout the entire visible spectrum. Fluence greater than 2.5 nC μm^{-2} results in the controlled writing of bulk silver on the surface, with a minimum line width as small as 400 nm and narrow gaps as small as 50 nm. The high ionic conductivity of the substrate is shown to be a vital component to the process, allowing the wide range of colors to be produced along with the controlled, nondendritic growth of silver structures.

1. Introduction

Silver nanoparticles display strong coupling in the visible spectrum due to the metal's high conductivity and bulk plasmon frequency in the ultraviolet.[1] Glasses containing silver have long been produced with the plasmonic resonance of silver nanoparticles imparting a yellow tint.[2] Silver plates, octahedra, cubes, and stars can all be made in solution synthesis techniques such that they absorb light throughout the visible spectrum.[3–5] These bottom-up approaches show remarkable control over particle size, but suspensions of these particles are difficult to deposit precisely on a surface, where interparticle interactions affect plasmonic resonance. In contrast, top-down silver film patterning techniques such as nanosphere lithography, microcontact printing, and solid-state superionic stamping allow for control of large arrays of particles in applications as transparent conductors and for light trapping in photovoltaics.[6–12] Moreover, silver substrates with a wide variety of colors have also been demonstrated in films with focused ion beam (FIB) milled holes and slits.[13,14] In addition to color filtering applications, silver structures have a wide variety of uses including plasmonic trapping, surface enhanced Raman spectroscopy (SERS), and plasmonic focusing.[15–18]

K. E. Jacobs, Prof. P. M. Ferreira
Department of Mechanical Science and Engineering
University of Illinois at Urbana-Champaign
1206 W. Green St, Urbana, IL 61801, USA
E-mail: pferreir@illinois.edu

DOI: 10.1002/adfm.201501965

Direct writing processes have the advantage of localized deposition, reduced number of process steps, and greater flexibility. Focused electron beam–induced deposition (FEBID) and focused ion beam–induced deposition (FIBID) are two prominent methods for localized metal deposition, where a precursor gas is adsorbed onto a substrate and subsequently decomposed by a charged particle beam. The vacuum chamber must be fitted with an insertion needle in order to introduce the gaseous precursors into the chamber close to the deposition area. Since precursors must have a sufficient vapor pressure to flow into the chamber, selection of the appropriate material can be challenging and precursors are often organometallics such as metal carbonyls or halogenophosphines.[19] A review by Botman highlights the difficulty in depositing pure metals, with deposited material consisting of small metal clusters in an amorphous carbon matrix.[20] Even more challenging is the lack of volatile precursor compound for silver.

An alternative to gas phase deposition is to inject a liquid silver precursor directly onto the substrate in a vacuum chamber. Bresin produced aqueous silver nitrate at low pressure both through hydration of solid precursor particles and with direct droplet injection.[21] While these techniques produced silver traces down to 70 nm in width, beam scattering caused by penetration through the liquid layer limited patterning to the small area where the liquid layer is thinnest. Even with the use of surfactants to produce a small contact angle, high-resolution patterning is limited to the few micrometers around the perimeter of the droplet. Ocola has demonstrated similar deposition from aqueous silver nitrate using a thin polyimide membrane to contain the liquid. Though this configuration allows flexibility in the location for direct writing of silver, the technique resulted in granular silver traces with significant nonspecific deposition.[22] Both of these techniques for producing a liquid precursor within a vacuum environment significantly increase the complexity of the process, while achieving modest success.

In contrast to both gaseous and liquid based precursors for direct writing of silver nanostructures, this work investigates an all-solid-state writing process that uses a solid-state ionically conductive substrate to supply silver by electrochemical extraction. Several silver compounds are known to have high room temperature ionic conductivity, most notably $RbAg_4I_5$.[23] However, the rapid decomposition of the material in the

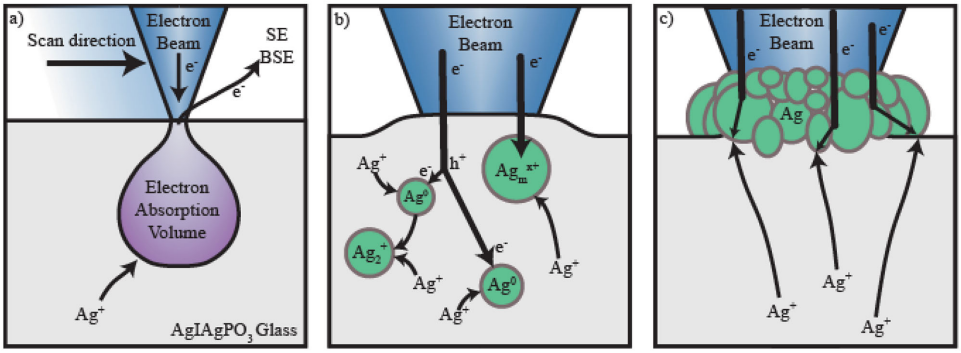

Figure 1. Schematic of the silver writing process. a) An electron beam scans the surface of the glass, with electrons depositing below the surface. Silver ions migrate to the deposition site neutralizing the charge buildup. b) Initially primary electrons generate electron–hole pairs which combine with local Ag^+ ions to form silver nanoparticles. Once the primary electron loses energy it also causes precipitation by reducing silver. c) When silver nanoparticles coalesce into a metal film thick enough to absorb the beam, film growth is only due to the absorbed electrons which drive electrochemical deposition.

presence of moisture makes its use as a substrate material impractical. Several silver oxyacid based compounds of the form $AgI_x(Ag_yMO_z)_{1-x}$ where M = P, As, Se, Te, Cr, Mo, and W have been found to be ionic conductors and are significantly less reactive to moisture compared to $RbAg_4I_5$.[24–29] In particular, the structure and tunability of the glass transition, activation energy, and ionic conductivity of $(AgI)_x(AgPO_3)_{1-x}$ glass mixtures have been well studied due to the wide transparent glass forming region from $x = 0$ to 0.6.[12,24,30] Addition of AgI to $AgPO_3$ increases the ionic conductivity from 4.2×10^{-6} S cm^{-1} for $AgPO_3$ to 3.2×10^{-2} S cm^{-1} for $AgIAgPO_3$ while both the glasses remain electrical insulators.[31] In this work, the superionic conductor $AgIAgPO_3$ was chosen to demonstrate the efficacy of an electron beam to extract silver from an ionically conductive substrate. To highlight the importance of ionic conduction to the process, the much less conductive glass $AgPO_3$, which is structurally similar to $AgIAgPO_3$, was also characterized. (See the Supporting Information for additional background information on the $(AgI)_x(AgPO_3)_{1-x}$ system.) The process presented results in modification of the glass surface composition, producing a rich color palette with high lateral resolution and with potential applications for storage media and product authentication. With increased electron fluence, we also demonstrate the capability to direct-write silver nanoparticles of various shapes on a transparent substrate.

2. Silver Particle Generation in Glass

Silver doped glasses have been shown to locally precipitate silver when subjected to excitation such as that from femtosecond lasers, gamma rays, and electrons when followed by thermal annealing.[32–36] After femtosecond direct laser writing (DLW) and heat treatment, silver doped zinc phosphate glass displays increased optical absorption below 450 nm due to the generation of several silver species and white fluorescence due to the development of Ag_m^{x+} nanoclusters.

In this process, the amplitude of the emission is proportional to the number of pulses applied and emission intensity–based multibit data storage has been demonstrated.[37] Bourhis describes the progression of this photochemical process in three steps. First, multiphoton absorption results in electrons elevated from the valence to conduction band within the matrix creating electron–hole pairs which are quickly captured by silver ions to form both neutral and charged silver species such as Ag^0 and Ag^{2+} via the reaction shown in Equation (1). Second, silver nanoclusters of Ag_m^{x+}, where typically $m < 20$ and $x < m$, are formed near the periphery of the treated area through a localized oxido-reduction clustering reaction shown in Equation (2). Finally, Ostwald ripening of the charged silver nanoclusters enlarges them to nanoparticles ranging from 5 to 15 nm.[38,39] Due to the low room temperature diffusion of silver species in these glasses however, this final step requires extended heating by the laser or a separate heat treatment near the glass transition temperature of the substrate.

$$2Ag^+ + e^- + h^+ \rightarrow Ag^{2+} + Ag^0 \quad (1)$$

$$Ag^+ + Ag^0 \rightarrow Ag_2^+, \quad Ag^+ + Ag_m^x \leftrightarrow Ag_{m+1}^{x+1} \quad (2)$$

Direct e-beam writing on an ionic conductor shares several similarities as well as an important distinction from the DLW process. **Figure 1**a shows an overview of the process, where the beam from a high-resolution scanning electron microscope (HRSEM) creates an interaction volume of mobile electrons in the substrate. Besides the energy associated with the beam, it also transfers a net current to the sample which is determined by the difference between the primary beam current and losses of secondary and backscattered electrons to the chamber. In the initial stage shown in Figure 1b, scattering of the primary beam generates secondary electrons which facilitate the creation of silver nanoclusters throughout the interaction volume, in a reduction and clustering process similar to DLW. However unlike the DLW process, the higher mobility of Ag^+ ions permits nanoparticle formation across the entire interaction volume, and not only at the boundaries. Moreover, the net negative charge deposited by the beam reduces the charge on particles and directly contributes to silver reduction as shown in Equation (3) resulting in increased silver deposition. Importantly, the high ionic conductivity of the substrate prevents surface charging by allowing Ag^+ ions migrate to the surface.

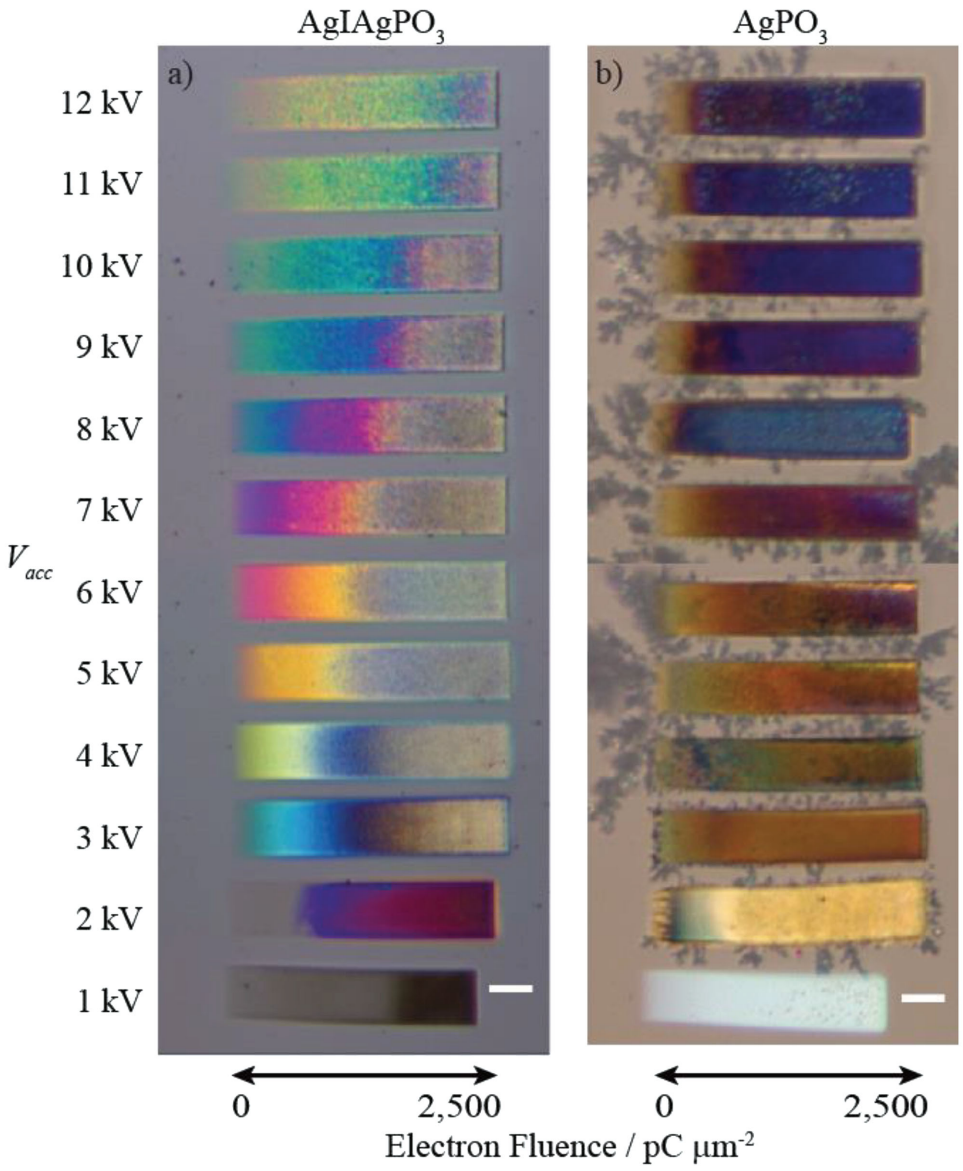

Figure 2. Color palettes produced on $AgIAgPO_3$ by electron beam irradiation. a) Optical image of $AgIAgPO_3$ patterned in a linear fluence gradient from left to right from 0 to 2500 pC μm^{-2}. From bottom to top the beam voltage is 1–12 kV. b) Image of $AgPO_3$ patterned in identical conditions showing dendritic growth and limited color palette. Scale bars are 10 μm.

As sufficient silver particles precipitate, they coalesce to form a film on the glass surface. When the film grows thicker than the beam penetration depth, as shown in Figure 1c, secondary electrons are no longer generated in the glass, and only direct silver reduction continues. At this point, further silver precipitation is restricted to the silver–substrate interface, which results in both vertical and lateral growth of the silver film

$$Ag_m^x + e^- \rightarrow Ag_m^{x-1} \quad (3)$$

3. Silver Painting

Figure 2a depicts the color induced in patterned areas of $AgIAgPO_3$ with varying accelerating voltages and electron fluence. At each voltage from 1 to 12 kV, a gradient of primary beam fluence was applied from 0 to 2500 pC μm^{-2}. At 1 kV, the large secondary electron emission from the surface causes a net positive charge to be deposited, resulting in no reduction of colored silver. At 2 kV, the electrons emitted from the surface nearly match those of the incoming beam, resulting in limited formation of silver nanoclusters. For 3 kV and above, the charge of the incoming beam exceeds the emitted charge, resulting in net deposition of electrons and the electrochemical reduction of silver. From left to right, the increasing fluence results in a shift in hue.

After a point, the patterned area loses saturation which is hypothesized to be due to the coalescence of isolated nanoparticles into a metallic film on the surface. Since higher voltage beams result in a wider range of electron penetration

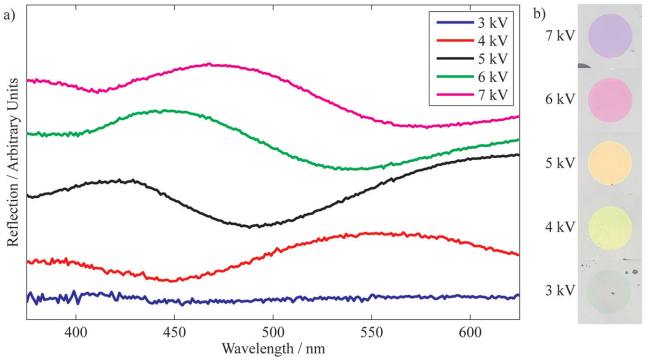

Figure 3. Reflection spectra of e-beam patterned dots. a) Total reflection spectra from dots patterned at 300 pC μm^{-2} and several voltages. Data are offset vertically for clarity. b) Optical images corresponding to the 225 μm diameter dots.

Figure 4. Microscope optical images on $AgIAgPO_3$ produced by patterned electron beam irradiation. a) Optical image of high-contrast bicolor graphic. Patterned in two passes: 5 and 7 kV V_{acc}. b) Optical image of gradient painting pattern in two passes: 4 and 6 kV V_{acc}. Scale bars are 25 μm.

depths, higher fluence is required to achieve coalescence at high voltages. The color seen at low fluence was observed to sweep the visible spectrum with increased acceleration voltage, suggesting either a difference in initial nanoparticle nucleation size, particle concentration, or alteration of the glass index near the surface due to beam energy.

For comparison, Figure 2b shows patterning performed on a nonsuperionic sample of silver metaphosphate. Whereas $AgIAgPO_3$ possesses a high room temperature ionic conductivity, the conductivity of $AgPO_3$ is four orders of magnitude smaller. Without adequate bulk conductivity, trapped charges accumulate during irradiation, resulting in long-lived charge trapping in the exposed areas and the development of a large electric potential between glass surface and the grounded stage to which it is attached. Doi and Asakura have demonstrated that in an electric field of 400–600 V cm^{-1}, $AgPO_3$ will undergo dielectric breakdown and grow silver dendrites though the bulk of the glass.[40] Indeed, $AgPO_3$ samples demonstrated dendritic growth of silver when subjected to 2–12 kV beams, conditions in which a net negative charge is transferred to the glass. The reduction of silver in the growth of uncontrolled dendrites consumes the surface charge, lowering the overall nanoparticle growth in the interaction volume. Moreover, the preference toward dendrite growth is accentuated in $AgPO_3$ due to the limited availability of Ag^+ ions near the surface compared to further in the bulk. The net result is the extremely limited color profile when compared to irradiated $AgIAgPO_3$. At high fluence, the penetration of the silver dendrites into the glass matrix generated enough stress to fracture the surrounding glass.

Specular data, shown in **Figure 3**, were gathered from larger dots patterned in $AgIAgPO_3$ with an electron fluence of 300 pC μm^{-2}. Dots were 225 μm to provide sufficient signal to collect specular data. The combined diffuse and specular reflection spectra show that at 3 kV, very little alteration is made in the visible range at this fluence. Beginning at 4 kV, the yellow color is revealed to be a pair of broad peaks in reflection appears across the visible range. This is in contrast to the extinction below 450 nm by the DLW process and the single fluorescence peak associated with it. With further increase in acceleration voltage, the spectrum remains qualitatively the same, but shifted toward longer wavelengths. This is consistent with the extracted silver resulting in a continuous change in the effective refractive index of the top layer along with increase in electron absorption depth with beam voltage.

Figure 4 demonstrates different approaches to patterning utilizing the available color palette. In Figure 4a, a high contrast bicolor optical image was produced using beams at 5 and 7 kV at fluences of 440 and 477 pC μm^{-2}, respectively. This method produces uniform colors over large areas and can produce vibrant submicrometer colored lines. Alternatively, in Figure 4b the image was produced using several levels of fluence from beams at 4 and 6 kV to produce more gradual color gradients. Since several accelerating voltages display several hues, only a few passes are required. Both methods are capable of positioning accuracy limited only by electron beam software and hardware.

4. Silver Film Growth and Surface Properties

Across all electron fluences, atomic force microscopy (AFM) scans show that the surface became raised in the patterned areas. **Figure 5** shows the results of writing bulk quantities of silver in the form of 4 × 4 and 2.5 × 2.5 μm squares, while varying accelerating voltage between 5, 7, and 10 kV. For each accelerating voltage, the electron fluence was set by varying the writing duration of the beam while at constant current. For doses up to 3–5 nC μm^{-2}, the thickness increased monotonically, with higher acceleration voltages resulting in faster deposition rates. Beyond 3–5 nC μm^{-2} the growth rate transitioned to a lower, linear rate of 0.012, 0.028, and 0.039 μm^3 nC^{-1} for voltages of 5, 7, and 10 kV, respectively (for data presented as growth rates, see Figure S1, Supporting Information). The clear decrease in film growth rate indicates a change in the dynamics of deposition. Monte Carlo simulations of a beam incident on a silver film show that the shift to a slower growth rate matches the maximum electron penetration depth (Figure S2, Supporting Information). This is consistent with the notion that once a thick layer of silver coats the substrate, secondary electrons generated in the silver are reabsorbed before reaching the underlying glass, causing the deposition rate only to be driven

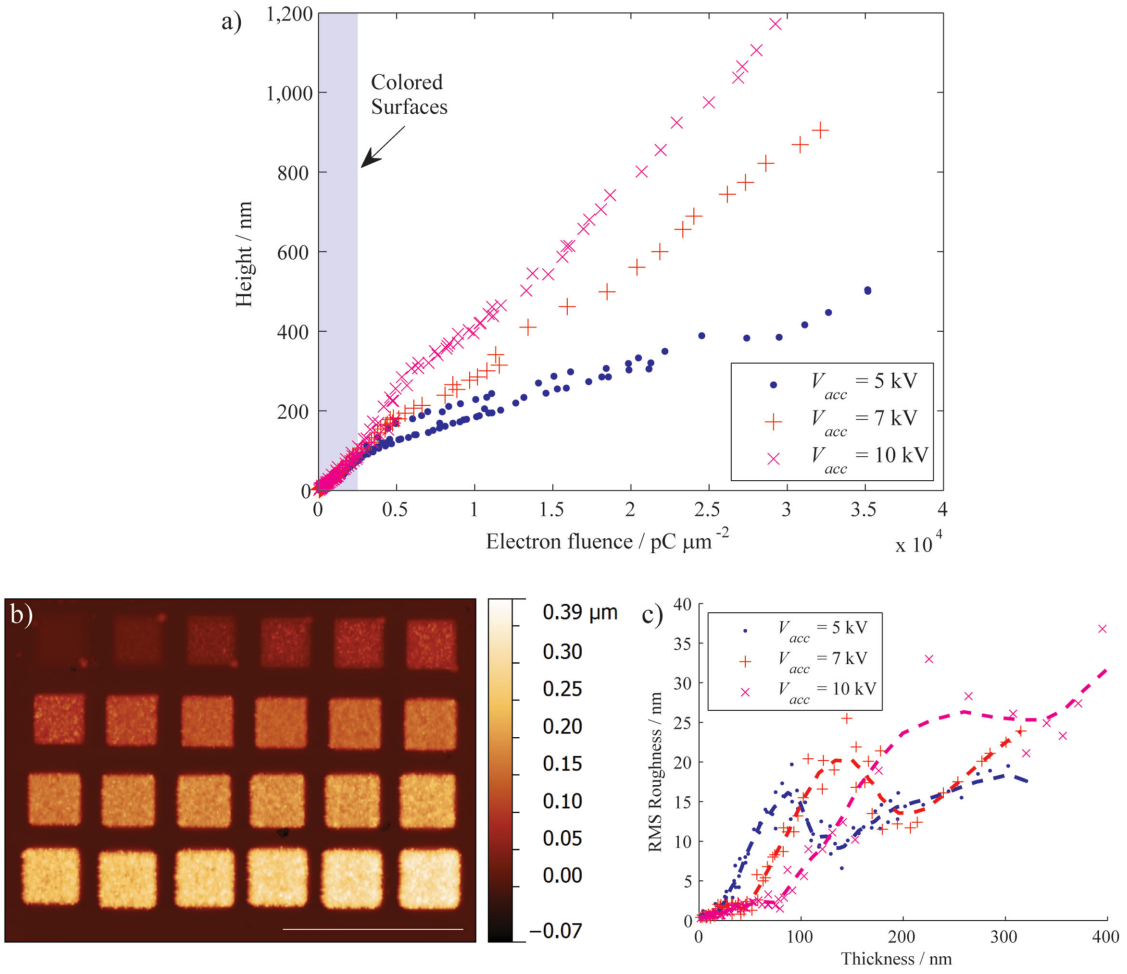

Figure 5. Silver growth with increasing electron fluence. a) Graph of thickness versus dose, b) AFM image of squares patterned at 5 kV from 0.5 to 21.3 nC μm^{-2}, and c) RMS roughness versus thickness. Moving average lines added to aid the eye. Scale bar is 10 μm.

by the charge absorbed by the silver film. In the high fluence regime, variation in deposition rate with acceleration voltage is consistent with lower total emitted electron efficiency at higher voltages. See Figure S3 (Supporting Information) for stage current yield on a reference sample of silver as a function of acceleration voltage.

The transition to a film of silver atop the glass substrate from subsurface nanoparticles is shown in Figure 5b,c. Morphologically, the writing process began with a uniform increase in surface height without large increases in surface roughness. As electron fluence was increased, silver grains became visible on the surface and coalesced to form a continuous metal film. The height at which grains became visible varied with acceleration voltage, where low voltage beams produced grains at the lowest fluence. This is consistent with Monte Carlo simulations which predict a widening of electron penetration distributions with increased acceleration voltage. While lower energy beams concentrate the initial silver deposition closer to the surface, high energy beams distribute silver deposition over a wider range of depths, requiring a higher fluence for the concentration of silver at the surface to reach the coalescence threshold.

AFM measurements also show an increase in the lateral size of patterns compared to the nominal dimensions. While some of this increase is due to the scattering effects of the beam within glass, features continue to spread even when the silver film is thick enough to absorb the beam. Since creation of thick films is driven electrochemically, deposition is not localized to the beam but to the entire area of the silver film, uniformly increasing film thickness.

Figure 6a demonstrates the lateral resolution of lines written at 5 kV and 3.9 nC μm^{-1}. Lines are 160 nm thick and 400 nm wide. At fluences above the transition to purely electrochemical deposition, pattern edges gain sharp contrast. Though beam scattering appears to limit the minimal achievable line width, the process displays much higher resolution in producing silver gaps. Since patterns grow laterally in the electrochemical regime, features can be grown such that gaps reach less than 60 nm. Figure 6b–d demonstrates structures spaced 50 nm apart, a bowtie antennae with a thickness of 215 nm and a gap of 55 nm, and a 150 nm wide NSOM aperture produced in an opaque 280 nm thick silver film. All nonpatterned areas remain optically transparent.

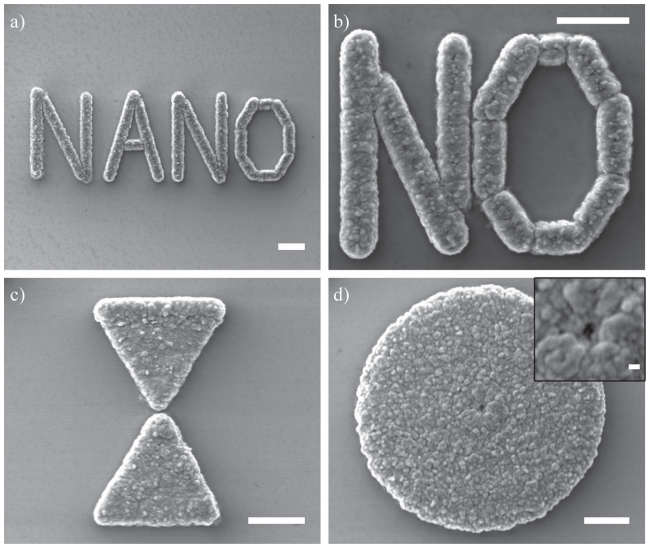

Figure 6. High-resolution silver structures patterned on $AgIAgPO_3$. a) Lateral resolution test of lines written at 5 kV and 3.9 nC μm^{-1}. b) Silver lines patterned with a 50 nm gap. c) Bowtie antennae with 55 nm gap. d) 150 nm NSOM aperture in 280 nm thick silver film. Scale bars 1 μm, inset scale bar 100 nm.

5. Thermal Analysis

In addition to initiating silver nanoparticle precipitation, the electron beam delivers thermal energy to the glass surface which may affect the process. Hiki, Takahashi, and Kogure measured the thermal conductivity at 40 °C of $AgPO_3$ and $AgIAgPO_3$ to be only 0.430 and 0.259 W m^{-1} K^{-1}, respectively, which suggests that heat may be poorly transferred away from the interaction volume, especially under high current patterning.[41] To estimate the expected steady-state temperature rise created by the electron beam, a 2D axisymmetric finite element model of the glass was made in COMSOL. The relevant glass domain modeled as a 10 μm radius × 10 μm deep cylinder modeled with a thermal conductivity reflecting that of $AgIAgPO_3$ or $AgPO_3$. Due to the increased absorption and higher thermal conductivity of silver during the process, a third simulation was conducted assuming the interaction volume consists of silver with $AgIAgPO_3$ as the surrounding material. Boundary conditions at the sides and base of the model were fixed at 20 °C, while the top surface was assumed to be thermally insulating.

Simulations were conducted for 3 nA beams corresponding to 5, 7, and 10 kV acceleration voltages. Heat generation from the electron beam interaction was assumed to be uniform within a hemispherical interaction volume. Total beam power was calculated in Equation (4) as a function of the energy carried by each electron and the primary beam current. The effective beam heating power can be calculated by considering the energy lost due to escaped secondary electrons as well as the slightly reduced energy carried away by backscattered electrons. However, the energetic contribution of lost secondary electrons is small, and the majority of backscattered electrons retain a significant portion of their initial energy. To simplify calculations, the effective beam heating power was calculated using Equation (5) by assuming backscattered electrons retained their initial energy. The backscattering coefficient, η, as well as the maximum penetration depth were obtained from Monte Carlo simulations and are shown in **Table 1**

$$P_{\text{total}} = \frac{E_{\text{electron}} I}{1.6\times10^{19}\,\text{C/e}^-} \tag{4}$$

$$P_{\text{thermal}} = (1-\eta)P_{\text{total}} \tag{5}$$

Figure 7 illustrates that since the glass was thermally insulating, heat was well confined to the interaction volume while the rest of the simulated volume remained near room temperature. The maximum temperatures in simulations of $AgIAgPO_3$ were 56.2, 48.1, and 42.9 °C, all below the glass transition temperature of the substrate. With a higher thermal conductivity and larger interaction volume, maximum temperatures reached in $AgPO_3$ are even lower. Considering that silver precipitation in the glass is likely to increase the thermal conductivity in the interaction volume, it seems likely that the electron beam thermal interaction with the glass does not significantly affect the process at the beam powers investigated.

6. Material Analysis

Energy-dispersive spectroscopy (EDS) was conducted on the glass before and after patterning at high fluence, with the results shown in **Table 2**. For reference, the spectrum of pure silver was measured as well as that of $AgIAgPO_3$. Due to carbon contamination in the chamber, a small amount of carbon was detected in all samples. To measure the glass prior to deposition, the spectrum of the glass was recorded at low magnification, reducing the electron fluence during measurement to a

Table 1. Summary of thermal beam power and resulting maximum temperatures from finite element simulation. Backscatter efficiency and maximum penetration depths calculated from Monte Carlo simulations.

		Beam accelerating voltages		
		5 kV	7 kV	10 kV
Primary beam power at 3 nA [μW]		15	21	30
Backscatter efficiency [η]	$AgPO_3$	0.269	0.262	0.28
	$AgIAgPO_3$	0.335	0.328	0.35
	Ag in $AgIAgPO_3$	0.364	0.368	0.390
Approximate penetration depth [nm]	$AgPO_3$	300	525	1000
	$AgIAgPO_3$	250	450	750
	Ag in $AgIAgPO_3$	120	200	360
Thermal dissipation power density [$\times10^{13}$ W m^{-3}]	$AgPO_3$	19.4	5.11	1.03
	$AgIAgPO_3$	30.5	7.39	2.64
	Ag in $AgIAgPO_3$	264	79.2	18.7
Maximum temperature [°C]	$AgPO_3$	39.9	35.8	31.2
	$AgIAgPO_3$	56.2	48.1	42.9
	Ag in $AgIAgPO_3$	68.4	60	50.2

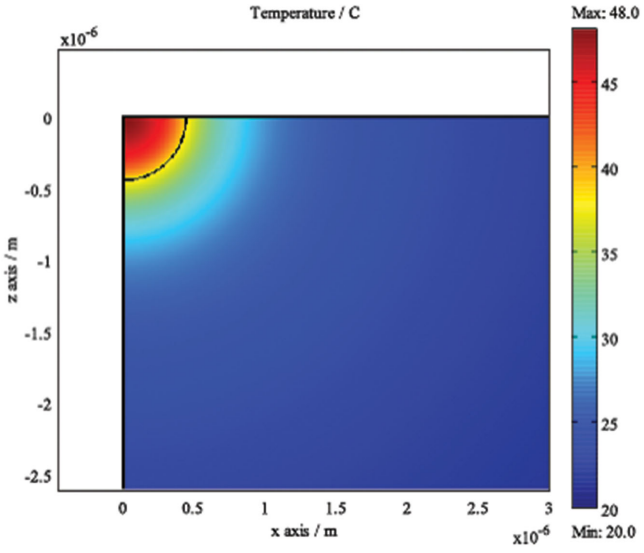

Figure 7. Finite element model of heating in $AgIAgPO_3$. Example simulation of the steady-state temperature rise due to thermal input from electron beam. The simplified thermal modeling assumes uniform power dissipation within a hemispherical interaction volume. With a 7 kV beam at 3 nA, there is less than a 28 °C temperature rise. Since this is still well below the substrate glass transition temperature of 81 °C, the process does not induce large-scale melting during irradiation.

negligible level. The unpatterned glass displayed strong silver, iodide, and phosphorous peaks, matching the expected ratios for $AgIAgPO_3$. Compared to the unpatterned glass, areas of glass patterned at 10 kV show more silver present, with iodide, phosphorus, and oxygen content suppressed. Chamber contamination, however, causes carbon content to rise slightly with increased beam dwell time. Unlike EBID deposition with carbon containing precursors, the carbon content of structures made in this process can be reduced through better chamber maintenance.

7. Conclusion

The effects of electron beam irradiation of a high ionic conductivity transparent glass, $AgIAgPO_3$, were investigated. The electron beam initiates precipitation of silver within the beam interaction volume leading to swelling of the surface. It was found that for fluences lower than 2500 pC μm^{-2} the surface exhibits strong coloration throughout the visible range. Though several papers have shown color change of phosphate glasses containing silver after local excitation, this is the first time such a change has been demonstrated that smoothly sweeps the entire visible range and requires no subsequent heat treatment. We attribute the immediate appearance of color to silver nanoparticle formation facilitated by the high room temperature mobility and concentration of Ag^+ ions present in $AgIAgPO_3$, in conjunction with direct injection of charge from the beam. Without high ionic conductivity, irradiation of $AgPO_3$ glass only produces a limited set of colors.

From AFM scans of the surface, surface modification due to the electron beam initially appeared as a raised surface with the process capable of fine control of surface height down to 1 nm average surface height for low fluence (<300 pC μm^{-2} at 5 kV). At sufficient electron fluence, the accumulated embedded silver particles coalesced into a film and broke through to the surface. Thick film formation of greater than 1 µm for high fluence (3000 pC μm^{-2} at 10 kV) was possible by electron capture and subsequent electrochemical growth of silver particles on the surface. Both the colored embedded silver nanoparticles and silver film on the surface were patterned in submicrometer features, with surface patterning displaying line width resolution of 400 nm and feature-to-feature spacing of less than 60 nm. Film growth characteristics were consistent with Monte Carlo simulations indicating that the process is controlled by both the energy and charge absorbed by the substrate from the electron beam.

This process displays several favorable characteristics for future applications. The patterns generated here may find use for high-resolution color applications including optical data storage and color security labeling, or systems requiring fine control of surface height. The ability to tailor silver nanostructures is especially suited to plasmonic applications requiring optically transparent substrates. Future work includes exploring similar glass compositions, and optimizing for environmental stability of both the glass and written structures such that high reliability, long-term patterning is practical.

Table 2. Energy-dispersive X-ray spectroscopy of $AgIAgPO_3$, e-beam extracted material, and bulk Ag reference.

	Ag [at%]	I [at%]	P [at%]	O [at%]	C [at%]
$AgIAgPO_3$	38.6	19.8	20.5	14	7.1
Extracted Ag	88.1	0.2	1.3	1.3	9.1
Bulk Ag	88.7	0	0	0.4	10.9

8. Experimental Section

The glass, $AgIAgPO_3$, was synthesized from reagent grade silver nitrate (99.995% from Salt Lake Metals), monobasic ammonium phosphate (99.99% from Sigma Aldrich), and silver iodide (99.9% from Alfa Aesar). First, stoichiometric amounts of silver nitrate and ammonium phosphate were heated slowly in an alumina crucible until the liquid finished giving off fumes, at which point the crucible was heated to 600 °C for 1 h. Next, the silver metaphosphate was quenched on an aluminum plate, before being mixed in a new alumina crucible with equimolar amounts of silver iodide at 600 °C for 1 h. Afterward, the glass melt was soaked in a borosilicate tube at 400 °C for 24 h to remove particles generated from the glass reaction with the alumina crucible. After slow cooling, the glass was melted on an aluminum holder that was previously sputtered with a 100 nm layer of silver to act as a sacrificial counter electrode to the electron beam. Flush with the base of the ring is an optical window, which allows illumination from below. A flat surface for patterning was created by melting the convex surface of the glass against an optical flat, cooling and separating the two parts. Silver metaphosphate was separately melted onto silver foil to provide a control sample of low ionic conductivity glass.

Writing was performed on an FEI Dual Beam 235 FIB using the electron column, with accelerating voltages ranging from 1 to 12 kV. A faraday cup was used to measure the beam current prior to each pattern, and the write time was adjusted to achieve the desired electron fluence. The beam currents for 1 and 2 kV were 980 and 1800 pA, respectively, and beam currents for 3–12 kV acceleration were measured to range

from 2.9 to 3.9 nA. Height data and AFM images were produced with an Asylum Cypher in tapping mode. Elemental analysis was performed on a JOEL JSM-6060LV scanning electron microscope with an Iridium Ultra EDS system from iXRF Systems. The bulk silver reference was a 99.99% silver pellet obtained from Kurt J. Lesker. Monte Carlo simulations were conducted using Win X-Ray, an extension of CASINO Monte Carlo software. Optical images were recorded with an optical microscope with maximum NA = 0.55, a Canon Rebel T3i using illumination from a high intensity halogen lamp, and a polytetrafluoroethylene disk for white balance calibration. Reflection spectra were obtained with a Cary 5000 UV–vis–IR spectrophotometer using an integrating sphere with a 200 μm diameter black aperture to mask all but the patterned area.

Supporting Information

Supporting Information is available from the Wiley Online Library or from the author.

Acknowledgements

This work was supported by NSF through Grant No. 1200780. The work was carried out in part in the Frederick Seitz Materials Research Laboratory Central Research Facilities, and the Micro-Nano Mechanical Systems Laboratory at University of Illinois. K.J. and P.F. designed the experiments, and discussed and interpreted the observations. K.J. performed the experiments, analyzed the data, and was primary author of the paper. P.F. directed the research and helped write and edit the paper.

Received: May 12, 2015
Revised: June 17, 2015
Published online: July 24, 2015

[1] A. Murray, W. L. Barnes, *Adv. Mater.* **2007**, *19*, 3771.
[2] T. P. Seward III, *J. Non-Cryst. Solids* **1980**, *40*, 499.
[3] B. Sharma, M. F. Cardinal, S. L. Kleinman, N. G. Greeneltch, R. R. Frontiera, M. G. Blaber, G. C. Schatz, R. P. Van Duyne, *MRS Bull.* **2013**, *38*, 615.
[4] Y. Sun, Y. Xia, *Science* **2002**, *298*, 2176.
[5] M. J. Mulvihill, X. Y. Ling, J. Henzie, P. Yang, *J. Am. Chem. Soc.* **2010**, *132*, 268.
[6] W. Wu, N. G. Tassi, *Nanoscale* **2014**, *6*, 7811.
[7] H. A. Atwater, A. Polman, *Nat. Mater.* **2010**, *9*, 205.
[8] S. Pillai, K. Catchpole, T. Trupke, M. Green, *J. Appl. Phys.* **2007**, *101*, 093105.
[9] J. C. Hulteen, D. A. Treichel, M. T. Smith, M. L. Duval, T. R. Jensen, R. P. Van Duyne, *J. Phys. Chem. B* **1999**, *103*, 3854.
[10] T. R. Jensen, M. D. Malinsky, C. L. Haynes, R. P. Van Duyne, *J. Phys. Chem. B* **2000**, *104*, 10549.
[11] S. Gout, J. Coulm, D. Léonard, F. Bessueille, *Appl. Surf. Sci.* **2014**, *307*, 716.
[12] K. E. Jacobs, K. H. Hsu, X. Han, A. Kumar, B. P. Azeredo, N. X. Fang, P. M. Ferreira, *Nanotechnology* **2011**, *22*, 425301.
[13] C. Genet, T. W. Ebbsen, *Nature* **2007**, *445*, 39.
[14] B. Zeng, Y. Gao, F. J. Bartoli, *Sci. Rep.* **2013**, *3*, 2840.
[15] C. Min, Z. Shen, J. Shen, Y. Zhang, H. Fang, G. Yuan, L. Du, S. Zhu, T. Lei, X. Yuan, *Nat. Commun.* **2013**, *4*, 2891.
[16] J. P. Camden, J. A. Dieringer, J. Zhao, R. P. Van Duyne, *Acc. Chem. Res.* **2008**, *41*, 1653.
[17] K. H. Hsu, N. Fang, K. Fung, *J. Raman Spectrosc.* **2015**, *46*, 59.
[18] Y. Q. Fu, X. L. Zhou, *Plasmonics* **2010**, *5*, 287.
[19] I. Utke, P. Hoffmann, J. Melngailis, *J. Vac. Sci. Technol., B: Microelectron. Nanometer Struct.—Process., Meas., Phenom.* **2008**, *26*, 1197.
[20] A. Botman, J. Mulders, C. Hagen, *Nanotechnology* **2009**, *20*, 372001.
[21] M. Bresin, A. Botman, S. Randolph, M. Straw, J. Hastings, *Microsc. Microanal.* **2014**, *20*, 376.
[22] L. E. Ocola, A. Joshi-Imre, C. Kessel, B. Chen, J. Park, D. Gosztola, R. Divan, *J. Vac. Sci. Technol., B: Microelectron. Nanometer Struct.—Process., Meas., Phenom.* **2012**, *30*, 06FF08.
[23] T. Takahashi, *J. Appl. Electrochem.* **1973**, *3*, 79.
[24] C. Tomasi, P. Mustarelli, A. Magistris, M. P. I. Garcia, *J. Non-Cryst. Solids* **2001**, *293*, 785.
[25] D. Pitzschke, J. Curda, M. Jansen, *Z. Naturforsch.* **2009**, *64b*, 891.
[26] D. Pitzschke, J. Curda, G. Cakmak, M. Jansen, *Z. Anorg. Allg. Chem.* **2008**, *634*, 1071.
[27] D. Pitzschke, J. Curda, M. Jansen, *Z. Anorg. Allg. Chem.* **2009**, *635*, 926.
[28] A. Mandanici, A. Raimondo, M. Federico, M. Cutroni, P. Mustarelli, C. Armellini, F. Rocca, *J. Non-Cryst. Solids* **2014**, *401*, 254.
[29] T. Takahashi, S. Ikeda, O. Yamamoto, *J. Electrochem. Soc.* **1973**, *120*, 647.
[30] E. Kartini, M. F. Collins, T. Priyanto, M. Yusuf, N. Indayaningsih, E. C. Svensson, S. J. Kennedy, *Phys. Rev. B* **2000**, *61*, 1036.
[31] S. Bhattacharya, D. Dutta, A. Ghosh, *Phys. Rev. B: Condens. Matter Mater. Phys.* **2006**, *73*, 104201.
[32] K. Bourhis, A. Royon, G. Papon, M. Bellec, Y. Petit, L. Canioni, M. Dussauze, V. Rodriguez, L. Binet, D. Caurant, M. Treguer, J. J. Videau, T. Cardinal, *Mater. Res. Bull.* **2013**, *48*, 1637.
[33] K. Bourhis, T. Cardinal, M. Treguer, J. J. Videau, A. Royon, L. Canioni, D. Talaga, M. Dussauze, V. Rodriques, L. Binet, D. Caurant, J. Choi, M. Richardson, *Advanced Photonics and Renewable Energy*, Optics Society of America, Washington, DC, USA **2010**.
[34] K. Bourhis, A. Royon, G. Papon, L. Canioni, N. Makria, Y. Petit, T. Cardinal, *J. Non-Cryst. Solids* **2013**, *377*, 142.
[35] J. Qiu, M. Shirai, T. Nakaya, J. Si, X. Jiang, C. Zhu, K. Hirao, *Appl. Phys. Lett.* **2002**, *81*, 3040.
[36] C. Maurel, T. Cardinal, M. Bellec, L. Canioni, B. Bousquet, M. Treguer, J. J. Videau, J. Choi, M. Richardson, *J. Lumin.* **2009**, *129*, 1514.
[37] A. Royon, K. Bourhis, M. Bellec, G. Papon, B. Bousquet, Y. Deshayes, T. Cardinal, L Canioni, *Adv. Mater.* **2010**, *22*, 5282.
[38] N. Marquestaut, Y. Petit, A. Royon, P. Mounaix, T. Cardinal, L. Canioni, *Adv. Funct. Mater.* **2014**, *24*, 5824.
[39] M. Bellec, A. Royon, B. Bousquet, K. Bourhis, M. Treguer, T. Cardinal, M. Richardson, L Canioni, *Opt. Express* **2009**, *17*, 10304.
[40] A. Doi, N. Asakura, *J. Mater. Sci.* **2001**, *36*, 3897.
[41] Y. Hiki, H. Takahashi, Y. Kogure, *Solid State Ionics* **1994**, *70*, 362.